Refining Machine Learning Potentials through Thermodynamic Theory of Phase Transitions

Paul Fuchs[a], Julija Zavadlav[a,b,1]

[a]*Multiscale Modeling of Fluid Materials, Technical University of Munich, Boltzmannstraße 15, Garching, 85748, Bavaria, Germany*
[b]*Atomistic Modeling Center, Munich Data Science Institute, Technical University of Munich, Walther-von-Dyck Straße 10, Garching, 85748, Bavaria, Germany*

Abstract

Foundational Machine Learning Potentials can resolve the accuracy and transferability limitations of classical force fields. They enable microscopic insights into material behavior through Molecular Dynamics simulations, which can crucially expedite material design and discovery. However, insufficiently broad and systematically biased reference data affect the predictive quality of the learned models. Often, these models exhibit significant deviations from experimentally observed phase transition temperatures, in the order of several hundred kelvins. Thus, fine-tuning is necessary to achieve adequate accuracy in many practical problems. This work proposes a fine-tuning strategy via top-down learning, directly correcting the wrongly predicted transition temperatures to match the experimental reference data. Our approach leverages the Differentiable Trajectory Reweighting algorithm to minimize the free energy differences between phases at the experimental target pressures and temperatures. We demonstrate that our approach can accurately correct the phase diagram of pure Titanium in a pressure range of up to 5 GPa, matching the experimental reference within tenths of kelvins and improving the liquid-state diffusion constant. Our approach is model-agnostic, applicable to multi-component systems with solid-solid and solid-liquid transitions, and compliant with top-down training on other experimental properties. Therefore, our approach can serve as an essential step towards highly accurate application-specific and foundational machine learning potentials.

*Corresponding author (julija.zavadlav@tum.de)

1. Introduction

Molecular Dynamics (MD) is an important tool to discover new alloys for catalysis and manufacturing, understand their behavior, and optimize production processes. For example, MD simulations provide microscopic insights into the thermal stability of high-entropy alloys [1] or how crystallization affects microstructure and mechanical properties [2, 3]. Efficient high-throughput MD simulations enable active-learning guided search of high-temperature alloys [4]. However, the typically employed classical potentials model interactions through simple functional forms with only a few tunable parameters. Therefore, these potentials may fail to accurately reproduce multiple material properties with the same parametrization [5]. More critically, parametrizations are not necessarily transferable across allotropes of the same element [6]. Thus, they can significantly fail to describe phase stability [6, 7] and consequently the chemical potential important for crystallization [8].

Machine Learning Potentials (MLPs) promise to overcome the limitations of classical force fields. MLPs offer significantly improved accuracy, closely reproducing costly ab initio computations [9–11], while remaining scalable to million-atom systems [10, 12]. Many MLPs have been tailored to specific metals and alloys [7, 13] through a typical workflow of dataset generation, parameter optimization, and model validation [14]. To cover a broad range of relevant system conformations, the datasets contain relaxed, stressed, and defective samples from multiple crystal structures, often generated with active learning and MD simulations at a wide range of temperatures [7, 13]. Still, when subsequently validated on phase stability predictions, the trained models only qualitatively reproduce experimental measurements but fail to match them closely within a magnitude of tens to hundreds of kelvins [7, 13, 14].

Foundational MLP approaches aim to extend property prediction through MD simulation to a much wider class of chemically diverse materials by training on even more diverse and extensive datasets [15–17]. However, these models can exhibit significant deviations from experimental measurements [18]. For example, melting temperatures are sometimes underestimated by several hundreds of kelvins [17].The reasons for the deviation of application-specific and foundation MLPs from experimental results are multifaceted. Especially for foundational models, biases in the dataset towards specific structures or compounds can manifest as model bias [18]. Moreover, even carefully created and extensive datasets might omit important system conformations related to rare events [19] or might suffer from systematic computational errors [20]. Even if these errors are addressed through extensive benchmarks [18, 19], practically affordable density-functional theory calculations are often insuffi-

ciently accurate to describe experimental measurements of complex material properties [13, 14, 21]. For example, different DFT functionals significantly over- or underestimate melting temperatures of many pure metals and semi-conductors, sometimes in magnitudes up to hundreds of kelvins [22–24]. In principle, transfer learning strategies that extend the DFT dataset with more accurate electronic structure methods could further increase the accuracy of the MLPs [25]. However, such methods significantly increase computational costs, which potentially render dataset generation, especially for foundational models or bulk systems, computationally intractable.

Instead of improving the underlying data quality, so-called top-down learning approaches ensure consistency with experiments by directly training MLPs to match experimental measurements [26–28]. However, experimentally observable quantities are not direct outputs of the MLP, unlike force and energy, but are typically obtained by averaging system properties over long MD simulations. Thus, top-down training requires more advanced algorithms, as directly applying automatic differentiation to such simulations does not guarantee meaningful gradients and might suffer from high memory requirements [26]. The model-agnostic DiffTRe [26] algorithm leverages statistical mechanics reweighting approaches [29, 30] to efficiently compute gradients for equilibrium observables. This computation remains efficient even when observables, such as fluctuation-based stiffness constants [26, 27] or free energies [28], require extensive sampling. For only a few specified experimental data points, top-down learning of complex MLPs is ill-posed. Purely top-down learned MLPs predict off-target properties with high uncertainty [26]. On the other hand, top-down training can be used to regularize or refine MLPs trained via Force Matching rather than for training MLPs from scratch. This combination can correct pretrained MLPs for discrepancies with experimental data without inducing a large deviation from the underlying reference data [27]. Previous work has shown that MLPs can be refined top-down to predict solid-solid phase transitions at a target temperature [31]. However, this approach is restricted to matching the free energy of linear models and is not directly applicable to solid-liquid phase transitions.

In this paper, we propose the model-agnostic Differentiable Transition Temperature Correction (DiffTTC) method to correct MLPs towards accurate predictions of phase diagrams. The DiffTTC method adjusts the MLP using the model-agnostic and flexible DiffTRe algorithm such that the free energy difference between pairs of phases at target temperatures and pressures fulfills the thermodynamic criterion of phase coexistence. As an example of titanium, we demonstrate that our algorithm can simultaneously correct for solid-solid and solid-liquid phase transitions. Moreover, we assess that the procedure does not degrade the MLP performance on out-of-target prop-

erties and can be applied with other previously reported DiffTRe training targets [27]. We evaluate our findings in the light of current foundational models, providing a path towards general-purpose MLPs that can predict complex material properties with high accuracy.

2. Methods

2.1. Transition Temperature Computation

We compute transition temperatures for the phase diagram using the thermodynamic theory of phase transitions and direct solid-liquid interface simulations. In thermodynamics, two phases I and II are in equilibrium if they have equal temperature T, pressure P, and chemical potential μ [32]. The chemical potential is directly related to the Gibbs free energy G via $\mu = NG(P, T, N)$, which is a function of pressure, temperature, and number of particles N [33]. Therefore, Free Energy-based approaches determine the coexistence temperature $\hat{T}$ and pressure $\hat{P}$ by solving the equation

$$G^{\mathrm{II}}(\hat{T}, \hat{P}) - G^{\mathrm{I}}(\hat{T}, \hat{P}) = \Delta G^{\mathrm{I} \rightarrow \mathrm{II}}(\hat{T}, \hat{P}) = 0. \tag{1}$$

These approaches typically employ two steps. First, the approaches compute the free energy difference between the phases at a reference pressure or temperature, for example, using the Pseudo-Critical path method [34] for solid-liquid transitions or the Frenkel-Ladd method [35] for solid-solid transitions (see next section). Second, the approaches then calculate the change in free energy with varying pressure or temperature for both phases, for example, using multi-state reweighting [36] or the Reversible Scaling method [37] (see next section). In combination, these steps efficiently scan the free energy difference for a wide range of temperatures or pressures.

Free energy calculations require multiple complicated and costly simulations. Especially the order-disorder transition in melting point calculations for (crystalline) solids is difficult to capture [34]. Therefore, alternative approaches have been proposed that dynamically estimate the stability of phases at different thermodynamic conditions [38]. High energy barriers might prevent phase transitions in simulation times accessible by MD and can cause effects such as supercooling and superheating. Thus, direct approaches often introduce point defects into the solid phase or simulate systems with solid-liquid interfaces [38]. Point defects and interfaces both lower the energy barriers of melting and crystallization [38]. Simulating an interfacial system at constant pressure and energy but variable temperature additionally allows the system to equilibrate, possibly reaching the transition temperature at which both phases coexist in equilibrium [32]. To reduce the contribution

4

of the interface to the total system pressure in an isoenthalpic-isobaric simulation, the system must be prepared such that the interface area is small compared to the dimensions of the box perpendicular to the interface [32]. Then, the melting temperature at a given pressure can be found within a few trial simulations.

We perform the coexistence simulations in LAMMPS [39] using our plugin `chetrain-deploy` [12]. More details on the coexistence simulations are summarized in Supplementary Note 3.

2.2. Non-equilibrium Free Energy Calculations

Thermodynamic integration estimates the free energies between two potentials u^{I} and u^{II} by defining a λ-dependent potential $u(\lambda)$ with $\lambda \in [0, 1]$, $u(\lambda = 0) = u^{\text{I}}$, $u(\lambda = 1) = u^{\text{II}}$ and computing the integral

$$\Delta F^{\text{I}\rightarrow\text{II}} = F^{\text{II}} - F^{\text{I}} = \int_0^1 \left\langle \frac{\partial u}{\partial \lambda} \right\rangle d\lambda = W_{\text{rev}} \tag{2}$$

equal to the reversible work W_{rev} [33, 40]. This integral can be approximated through numerical quadrature. However, running multiple simulations to estimate the mean generalized force $\left\langle \frac{\partial u}{\partial \lambda} \right\rangle$ can be quite costly. Therefore, non-equilibrium approaches [40] approximate the reversible work by driving the system from $\lambda(0) = 0$ to $\lambda(t_s) = 1$ within a finite time t_s to obtain the irreversible work W_{irr} as an upper bound

$$W_{\text{rev}} \leq \int_0^{t_s} \dot{\lambda}(t) \frac{\partial H}{\partial \lambda(t)} dt = W_{\text{irr}}^{\text{I}\rightarrow\text{II}}, \tag{3}$$

where H is the Hamiltonian, equal to the sum of kinetic and potential energy of the system. Similarly, driving the process backward provides a lower bound of the reversible work. If performed sufficiently slowly, both processes result in an unbiased estimator $W_{\text{rev}} = \left(\langle W_{\text{irr}}^{\text{I}\rightarrow\text{II}} \rangle - \langle W_{\text{irr}}^{\text{II}\rightarrow\text{I}} \rangle \right)/2$ [40].

The Frenkel-Ladd approach [35] is an efficient method for computing absolute free energies of crystalline solid phases and, consequently, the free energy difference between the phases. The approach constructs a potential transformation from the target potential to that of an Einstein Crystal, in which the N particles with position $\mathbf{r}$ are harmonically coupled with a spring constant k_E to their lattice position $\boldsymbol{r}_0$ via the potential $u(\lambda = 1) = \sum_{i=1}^N k_E(\mathbf{r} - \mathbf{r}_0)^2/2$. For this simple potential, the absolute free energy can be computed analytically. Thus, the sum of the absolute free energy of the Einstein and the free energy difference to the target potential results in the absolute free energy of the target crystal. The Reversible

Scaling path [37] provides the free energy change across multiple temperatures within a single simulation for each phase at constant pressure. Thus, a single simulation for each phase is sufficient to find the coexistence temperature that solves equation (1). Conceptually, the method maintains a constant simulation temperature T^{I} but effectively scales the temperature to $T(\lambda) = T^{\mathrm{I}}/\lambda$ by scaling the potential to $u(\lambda) = \lambda u^{\mathrm{I}}$. Non-equilibrium thermodynamic integration along λ then results in the λ-dependent free energy $\Delta \tilde{G}^{\mathrm{I} \to \lambda}$, which can be connected to temperature change in free energy via $\Delta G(T) = \Delta \tilde{G}^{\mathrm{I} \to \lambda(T)}/\lambda + 3Nk_B T \log \lambda / 2$.

We perform the non-equilibrium simulations in LAMMPS [39] using our plugin `chetrain-deploy` [12], following the implementation from Freitas et al. [41]. More details on the free energy integrations are summarized in Supplementary Note 4.

2.3. Machine Learning Potential

MLPs are a class of parametric models with parameters θ that derive forces $\boldsymbol{f} = -\frac{\partial u_\theta(\boldsymbol{r})}{\partial \boldsymbol{r}}$ from a potential function $u_\theta(\boldsymbol{r})$ that depends on all particle positions $\boldsymbol{r}$ [42]. Often, the model architectures encode physical invariances, such as translational, rotational, and permutation invariance by design [42]. Descriptor-based potential, such as the DP model [9], ensures these invariances by encoding particle environments in invariant but often hand-crafted descriptors before feeding them particle-wise into general regression models such as fully connected neural networks. More recent equivariant graph neural networks [43] learn these environment descriptors from data by performing message-passing between particles within a maximum cutoff distance. Therefore, multiple message-passing operations propagate information beyond the cutoff, allowing the model to efficiently capture interactions between more distant particles. Moreover, all operations are constructed such that the final descriptors remain invariant. Therefore, these message-passing models provide the means to learn interatomic potentials purely from data. Still, additive repulsive prior potentials have been shown to improve simulation stability, especially at high pressures [15], and are thus often added to the model.

In this paper, we use an adapted version of the MACE [11] model. MACE correlates local features to effectively construct high-order many-body messages. Therefore, only two message-passing iterations are sufficient to obtain a highly descriptive and efficiently parallelizable model [11]. Unlike the original paper, we only use the output of the last, non-linear readout layer to learn the potential. To improve the simulation stability, we combine the

model with the pairwise Lennard-Jones potential

$$u_{\mathrm{LJ}}(\boldsymbol{r}) = \sum_{i=1}^{N} \sum_{j=1}^{N} 4\epsilon \left[\left(\frac{\sigma}{\|\boldsymbol{r}_i - \boldsymbol{r}_j\|} \right)^{12} - \left(\frac{\sigma}{\|\boldsymbol{r}_i - \boldsymbol{r}_j\|} \right)^{6} \right] \tag{4}$$

as an additive prior, where we infer the length scale σ from the BCC lattice parameter $a = 0.325$ nm (see Wen et al. [7] for comparison) via $2\sqrt[6]{2}\sigma = \sqrt{3}a$ and choose $\epsilon = 0.5$ kJ $\cdot$ mol.

We pretrain the MLP using the Force Matching method [12, 44] based on the curated dataset (see Supplementary information of Röcken and Zavadlav [27]) from Wen et al. [7]. Therefore, we minimize the mean squared differences of the potential $u_\theta(\mathbf{h}_i, \tilde{\mathbf{r}}_i)$, force $\mathbf{f}_\theta(\mathbf{h}_i, \tilde{\mathbf{r}}_i) = -\frac{\partial u(\mathbf{h}_i, \tilde{\mathbf{r}}_i)}{\partial (\mathbf{h}_i \tilde{\mathbf{r}}_i)}$ and stress $\sigma_\theta(\mathbf{h}_i, \tilde{\mathbf{r}}_i) = \frac{1}{\det \mathbf{h}_i} \frac{\partial u(\mathbf{h}_i, \tilde{\mathbf{r}}_i)}{\partial \mathbf{h}_i} \cdot \mathbf{h}_i$ [33] to the DFT reference data $\hat{u}_i, \hat{\mathbf{f}}_i, \hat{\sigma}_i$, predicted for the cell matrices $\mathbf{h}_i$ and fractional coordinates $\tilde{\mathbf{r}}_i$. Thus, the loss function reads

$$\mathcal{L}(\theta) = \frac{1}{D} \sum_{i=1}^{D} \left[\gamma_u \|u_\theta(\mathbf{h}_i, \tilde{\mathbf{r}}_i) - \hat{u}_i\|^2 + \frac{\gamma_f}{3N_i} \|\mathbf{f}_\theta(\mathbf{h}_i, \tilde{\mathbf{r}}_i) - \hat{\mathbf{f}}_i\|^2 \right.$$
$$\left. + w_i \frac{\gamma_\sigma}{9} \|\sigma_\theta(\mathbf{h}_i, \tilde{\mathbf{r}}_i) - \hat{\sigma}_i\|^2 \right], \tag{5}$$

where D denotes the number of training samples. The coefficients γ_u, $\gamma_{\mathbf{f}}$, and γ_σ balance the contribution of each quantity. We consider the virial only for uniformly strained samples by defining weights w_i which are non-zero only for these specific samples and sum up to $\sum_{i=1}^{D} w_i = D$. Details on the pretraining are summarized in Supplementary Note 1.

2.4. Differentiable Transition Temperature Correction (DiffTTC)

The pretrained model, to which parameters we will refer to in the following as θ_0, would correctly predict the transition temperature between phases if equation (1) is fulfilled at the experimentally determined coexistence point. In the DiffTTC method, we therefore adjust the model's parameters to correct the predicted transition temperatures by minimizing the magnitude of the predicted difference $\Delta G_\theta^{\mathrm{I} \rightarrow \mathrm{II}}(T_{\exp}, P_{\exp}) \xrightarrow{\theta} 0$ at the experimental coexistence point. To avoid first-order phase transitions and more complicated isobaric simulations, we adjust the Gibbs free energy by adjusting the Helmholtz free energy F. If the refined MLP predicts the same molar volume $V^{\mathrm{I/II}}/N$ as the pretrained MLP, the Gibbs and Helmholtz free energies change equally, i.e., $\Delta G_{\theta_0 \rightarrow \theta}^{\mathrm{I/II}} = \Delta F_{\theta_0 \rightarrow \theta}^{\mathrm{I/II}}$. Hence, for each pair of phases I and II, we aim to minimize the loss

$$\mathcal{L}(\theta) = \gamma_F \left(\Delta F_{\theta_0 \rightarrow \theta}^{\mathrm{II}} - \Delta F_{\theta_0 \rightarrow \theta}^{\mathrm{I}} + \Delta G_{\theta_0}^{\mathrm{I} \rightarrow \mathrm{II}} \right)^2$$
$$+ \gamma_P \left(P_\theta^{\mathrm{I}} - P_{\exp} \right)^2 + \gamma_P \left(P_\theta^{\mathrm{II}} - P_{\exp} \right)^2, \tag{6}$$

where $P_\theta^{\text{I/II}} = \langle p_\theta \rangle^{\text{I/II}}$ defines the ensemble average $\langle \cdot \rangle_\theta$ of the instantaneous pressure p_θ over the canonical distribution $\rho_\theta(\boldsymbol{r}) \propto \exp(-\beta u_\theta(\boldsymbol{r}))$ at temperature $\beta = (k_B T)^{-1}$ (k_B is the Boltzmann constant) and volume $V^{\text{I/II}}$. The loss penalizes changes in the average pressure, where coefficients γ_P and γ_F control the penalty strength compared to the free energy target. The volumes $V^{\text{I/II}}$ and initial difference $\Delta G_{\theta_0}^{\text{I}\to\text{II}}$ are constants that have to be estimated only once prior to the DiffTTC method.

We optimize the loss using the Differentiable Trajectory Reweighting (DiffTRe) algorithm [26]. The DiffTRe algorithm expresses the ensemble averages of a quantity a over the canonical distribution ρ_θ as weighted ensemble averages

$$\langle a(\boldsymbol{r}) \rangle_\theta = \langle w_\theta(\mathbf{r}) a(\mathbf{r}) \rangle_{\tilde{\theta}} \tag{7}$$

over the distribution $\rho(\boldsymbol{r})_{\tilde{\theta}}$ with MLP reference parameters $\tilde{\theta}$, leading to the weights

$$w_\theta(\mathbf{r}) = \frac{\exp\left(-\beta \left[u_\theta(\mathbf{r}) - u_{\tilde{u}}(\mathbf{r})\right]\right)}{\langle \exp\left(-\beta \left[u_\theta(\mathbf{r}) - u_{\tilde{u}}(\mathbf{r})\right]\right) \rangle_{\tilde{\theta}}}. \tag{8}$$

The algorithm then approximates the ensemble averages by drawing S samples in an MD simulation and computing gradients through automatic differentiation. Since only the weights and the instantaneous predictions, but not the sampled conformations, depend on θ, the algorithm avoids propagating gradients through the simulation. Moreover, DiffTRe reuses samples drawn in a previous simulation for multiple parameter updates if the effective sample size [45]

$$S_{\text{eff}} = \exp(-\sum_{i=1}^{S} w_i \log w_i), \tag{9}$$

measuring the statistical error of the approximation, remains above a predefined threshold $f < S_{\text{eff}}/S$. If the effective sample size exceeds the defined threshold during the parameter update, DiffTRe updates the reference parameters $\tilde{\theta} \leftarrow \theta$ to the current parameters and draws new samples. This resampling step limits the error in the predicted pressure, as resampling leads to equal weights, and fluctuation of the pressure samples depends only on the current potential. However, if the free energy is expressed as a simple ensemble average through the forward free energy perturbation estimator [29]

$$\Delta F_{\theta_0 \to \theta}^{\text{I/II}} = -\frac{1}{\beta} \left\langle \exp\left(-\beta \left[u_\theta - u_{\theta_0}\right]\right) \right\rangle_{\theta_0}, \tag{10}$$

8

only a few samples with a large negative difference effectively contribute to the prediction if the difference between the current and reference potential becomes large. Thus, the error in the predicted free energy difference can remain high even after resampling. We circumvent this problem through the concept of thermodynamic integration as proposed in the ReSolv method [28]. The sequence of parameters $\theta[i]$, each connected to a trajectory, forms a thermodynamic integration path from the initial potential $\theta[0] = \theta_0$ to the current potential. Thus, a more accurate differentiable estimator of the free energy can be obtained via the decomposition

$$\Delta F_{\theta_0 \to \theta}^{\text{I/II}} = \Delta F_{\theta[n] \to \theta}^{\text{I/II}} + \sum_{i=0}^{n-1} \Delta F_{\theta[i] \to \theta[i+1]}^{\text{I/II}}. \tag{11}$$

The free energy difference $\Delta F_{\theta[n] \to \theta}^{\text{I/II}}$ between the current parametrization θ and the most recent parametrization used to generate a trajectory $\theta[n]$ can be expressed via the forward-perturbation free energy estimator in equation (10). The other differences $\Delta F_{\theta[i] \to \theta[i+1]}^{\text{I/II}}$ can be computed immediately after each trajectory recomputation using, e.g., the more accurate Bennet Acceptance Ratio method [46].

The ReSolv method and the DiffTRe method can train arbitrary MLPs to match pressures and target free energy differences. However, our loss in equation (6) minimizes the free energy differences between two phases rather than fixed references. Nevertheless, under first-order optimization of the loss, the gradients with respect to both phases I and II can be computed independently. Therefore, we define the statepoint loss

$$\mathcal{L}^{\text{I/II}}(\theta) = \gamma_F \left(\Delta F_{\theta_0 \to \theta}^{\text{I/II}} - \Delta \hat{F}^{\text{I/II}} \right)^2 + \gamma_P \left(P_\theta^{\text{I/II}} - P_{\text{exp}} \right)^2, \tag{12}$$

and update the free-energy targets before each optimization step to

$$\Delta \hat{F}^{\text{I/II}} = \Delta F_{\theta_0 \to \theta}^{\text{II/I}} \pm \Delta G_{\theta_0}^{\text{I} \to \text{II}}. \tag{13}$$

When neglecting the gradients of $\Delta \hat{F}^{\text{I/II}}$, the sum of statepoint loss gradients $\nabla \mathcal{L}^{\text{I}} + \nabla \mathcal{L}^{\text{II}} = \nabla \mathcal{L}$ equals the gradients of the original loss function in equation (6).

In summary, correcting the transition temperature with the DiffTCC method, as outlined in Figure 1, consists of the following steps: The procedure begins with a pre-trained MLP, obtained, for example, via Force Matching in equation (5) (Step 1). The free energy differences between K pairs of phases $\{(\text{I}, \text{II})_i\}_{i=1}^K$ with average volumes $V_i^{\text{I/II}}$ at corresponding pressures P_i and temperatures T_i serve as training objectives. Thus, the quantities must

be predicted beforehand (Step 2) but only once, as they remain constant during the optimization. The DiffTRe algorithm iteratively updates the parameters to minimize the average loss in equation (6) for all statepoints (Step 3). Therefore, the algorithm samples a batch of statepoint pairs and predicts the current free energy targets in equation (13). If the effective sample size in equation (9) exceeds a predefined threshold of 0.9, similar to that in Thaler and Zavadlav [26], for any statepoint in the batch, the DiffTRe algorithm recomputes trajectories for all statepoints in the batch. Therefore, the algorithm runs short simulations of the pure phases in the NVT ensemble. After recomputation or if the effective sample size is within the threshold, the algorithm computes the batch average statepoint loss, as given in equation (12). Finally, the algorithm updates the potential parameters using a first-order optimizer, such as ADAM [47].
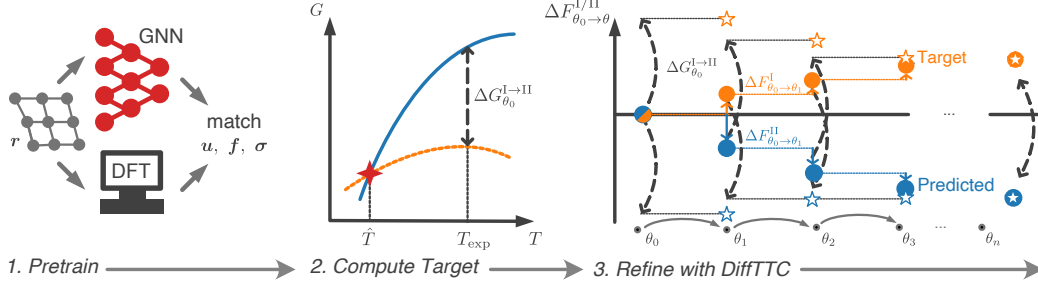

Figure 1: **Differentiable Transition Temperature Correction (DiffTTC) Method.** 1. The method begins with a pre-trained potential. 2. Using the pretrained model with parameters θ_0, the free energy difference $\Delta G_{\theta_0}^{\mathrm{I} \rightarrow \mathrm{II}}$ between phases I (blue line) and II (orange line) at the experimental transition temperature $T_{\exp}$ is computed, e.g., by extrapolating the phase free energy change in temperature from the coexistence point (red star) at $\hat{T}$. 3. DiffTTC corrects the melting temperature by iteratively refining the potential parameter θ, by matching the free energy changes $\Delta F_{\theta_0 \rightarrow \theta}^{\mathrm{I}/\mathrm{II}}$ (orange and blue points) towards dynamically adjusted targets (orange and blue stars), eventually compensating the initial free energy difference (dashed arrow).

We use the DiffTTC method to refine the pre-trained MLP from Section 2.3. Therefore, we run the algorithm for 250 epochs with batches of 6 pairs on a single A100 GPU. More details on the optimization hyperparameters and convergence are given in Supplementary Note 2.

3. Results

We benchmark our method by correcting a pretrained MLP as described in Section 2.3 using the DiffTTC method as described in Section 2.4 based on experimentally determined phase stability data for pure Titanium (see Wen et al. [7]).

3.1. Force and Energy Predictions

First, we evaluate how the refinement affects the predicted forces and energies of the MLP in comparison to the DFT reference data, summarized in Table 1. The pretrained model matches the DFT reference with an energy error within a magnitude of several meV and force error within a magnitude of tens meV Å^{-1}. These error magnitudes are commonly reported for MLPs [19, 20]. More specifically, the energy and force errors of our pre-trained model are comparable to those of the MLP presented by Röcken and Zavadlav [27], which was trained on the same dataset. Thus, the pretrained model serves as a reasonable baseline for the DiffTTC method.

Table 1: Mean absolute errors of energies, forces, and virial on the test split of the curated [27] DFT dataset from Wen et al. [7].

Quantity	Pretrained	Refined
Energy [meV atom^{-1}]	3.9	21.7
Force [meV A^{-1}]	69.0	84.1
Virial [meV atom^{-1}]	26.3	37.8

For the DiffTTC-refined model, the energy, force, and virial errors are higher compared to the pretrained model, as expected. Notably, the energy errors are approximately half a magnitude higher than those of the pretrained model, while the force errors only increase by around 20 %. This difference can be due to the importance of energy in the long-term stability of phases. Slightly decreasing the energy for, e.g., the solid-state structures compared to liquid structures increases their relative probability. If this change is approximately similar for all structures of a phase, the gradient of the energy mostly changes for rarely sampled transition states between the phases (see Thaler et al. [48], Figure 1, as an example illustration).

To assess the difference in force and energy predictions in more detail, we visualize them in Figure 2 with respect to the DFT reference. The energy and force magnitudes are slightly higher, scaled by a factor around 1 %. This scaling reinforces a higher energy for liquid structures compared to crystal structures and can decrease the relative probability of non-crystal structures. In addition to the scaling, lower energies are predicted for BCC structures, while higher energies are predicted for HCP structures. Thus, we expect that the stability of BCC structures is strengthened compared to HCP structures. The direction of the predicted force changes only slightly, except for small force magnitudes, where even slight changes in the predicted forces can significantly alter the direction.
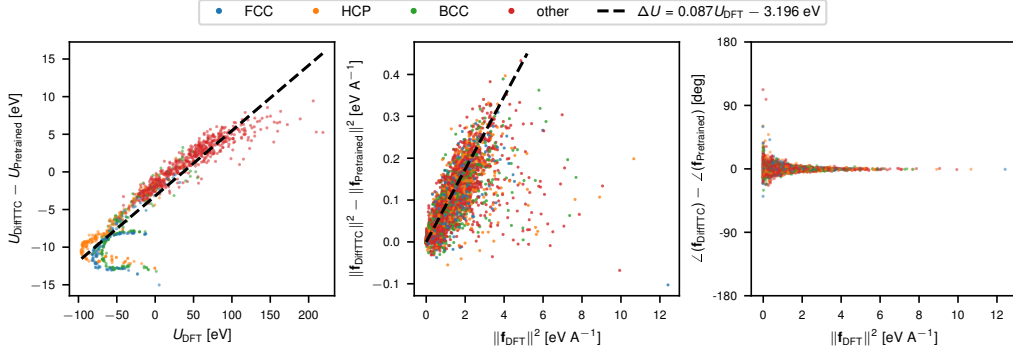
11

Figure 2: **Predicted Energies and Forces:** Differences in the predicted energy and forces between the pretrained and the DiffTTC-refined model on the test split versus the DFT reference energy. The right plot shows the angle of predicted forces with respect to the DFT force. The black dashed line in the left plot corresponds to a linear regression fit to the energy differences. The color corresponds to the dominant crystal structure identified via the polyhedral template matching method [49]. Only every 70th force component is shown.

3.2. Predicted Phase Diagram

To assess how the DiffTTC training affects the stability of phases, we compute the phase diagrams predicted by the pretrained and refined models through solid-liquid coexistence simulations and non-equilibrium free energy integrations (see Supplementary Notes 1 and 2). Figure 3 shows the predicted phase diagram for 6 pressures equally spaced between 0 and 5 GPa in comparison to the reference data. Details on the error estimates are given in Supplementary Note 5.

The phase diagram of the pretrained MLP aligns qualitatively roughly with the experimental reference. Reference and predicted slopes of the HCP-BCC and BCC-Liquid phase boundaries closely agree. According to the Clapeyron relation [32], this agreement indicates that the model approximately captures the molar volume difference between the phases. However, the absolute temperatures are predicted to be about 100 to 150 K lower for the HCP-BCC transition and about 200 K lower for the BCC-liquid transition than the experimental data.

This discrepancy can derive from inaccuracies in the reference DFT data. Commonly used DFT functionals over- or underestimate melting temperatures by magnitudes sometimes up to 200 K [22–24]. Optimally, with regard to the force matching objective, the MLP exactly reproduces DFT computations and therefore inherits these inconsistencies. However, even if MLPs reproduce diverse DFT data with low errors, the MLP and DFT force and energy predictions might differ for rarely encountered samples, leading to deviations in predicted material properties [19]. To assess this variability,
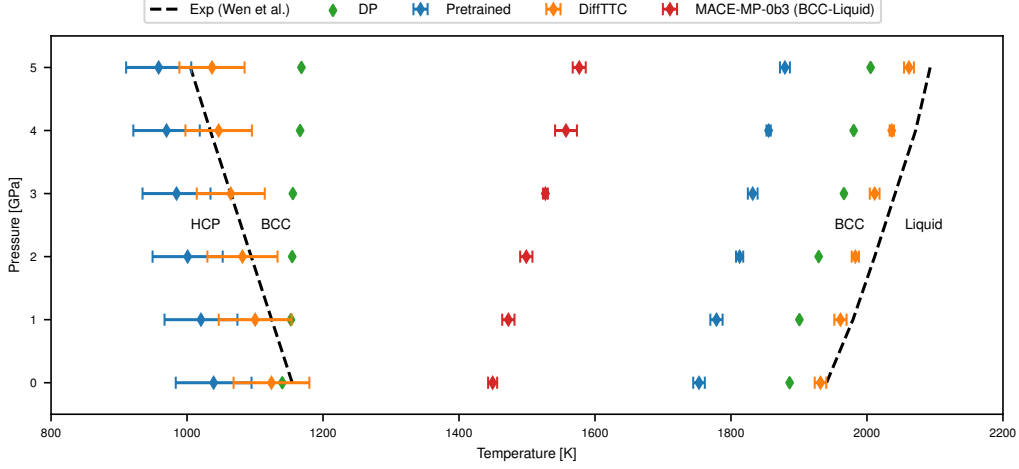
Figure 3: **Phase-diagram:** Predictions of the pretrained and through DiffTTC refined MACE model are shown in comparison to the DP model [7], the foundational MACE-MP-0b3 model [15] (only BCC-liquid phase transition), and experimental measurements. The values for the DP model and the experimental data (black dashed lines) are extracted from Wen et al. [7]. The error bars denote the uncertainty in the mean temperature in the coexistence simulations for the BCC-liquid transition and approximate the error in temperature of the free energy intersection point for the HCP-BCC transition based on error estimates reported in Freitas et al. [41] for the free energy integration methods.

we compare our pretrained baseline to the DP model reported in Wen et al. [7], which was selected and finetuned on extended DFT data from an ensemble of candidates based on its best overall test set performance (see Röcken and Zavadlav [27], Supplementary Information, for a description of the differences in the data). For the BCC-liquid phase boundary, the DP model trained on the same DFT dataset exhibits closer agreement to experimental measurements than the pretrained model, but still understimates the transition temperature. On the other hand, the HCP-BCC phase boundary predicted by the DP model differs significantly more from the experimental reference than the boundary predicted by our pretrained and refined model. The difference in the predicted phase diagram might derive from a higher preference for the energy error over the force error [50]. However, additional included structures and a different model architecture can also affect how the model interpolates unseen samples. Nevertheless, the pretrained model and the DP model show pronounced differences from the experimental reference. Thus, the results for the DP model emphasize that even for carefully designed project-specific datasets, additional refinement is necessary to achieve consistency with experiments.

We also test the foundational MACE-MP-03b model [15] to assess the

out-of-the-box performance of models trained on large and diverse datasets. Therefore, we calculate the BCC-liquid transition temperatures using the coexistence method as for our pretrained model, although with more than 50 % reduced interface area due to computational constraints. Notably, the simulations still ran for around 12 h, compared to less than 4 h for our simplified MACE models, on a single A100 (80 GB) GPU. The foundational model predicts a melting temperature more than 400 K lower than the experimentally measured value. This discrepancy is several hundred kelvins larger than the discrepancy between different experimental measurements [51, 52] (see Supplementary Figure S4 for a comparison). Nevertheless, all simulations, even at high temperatures and pressures, have been stable and have led to a slope of the phase diagram similar to the experimental reference. These observations agree with previous studies on the accuracy of thermodynamic properties predicted by foundational models. Although these MLPs show promising out-of-the-box performance on many computational benchmarks, they often cannot accurately capture complex material behavior [18]. Reasons for these failures include dataset biases towards specific compounds and structures [18]. Moreover, issues such as underrepresented important samples [19], which have been identified in application-specific datasets, are also likely to exist. Thus, benchmarking these models on diverse predicted properties involving MD simulations or, even more, fine-tuning these properties to experimental data, as proposed in this work, can be crucial for obtaining adequately accurate foundational models.

Finally, we evaluate the phase diagram of the model refined by DiffTTC. The DiffTTC-refined model predicts a phase diagram closely agreeing with the experimental reference, noticeably outperforming all other presented models. For both transitions, the temperature is predicted within less than 50 K of the experimental reference. For the HCP-BCC transition, the prediction agrees best at around 3 GPa, while the temperature is slightly overestimated at higher pressures and slightly underestimated at lower pressures. For the BCC-liquid transition, the temperature is predicted best at 0 GPa and increasingly underestimated for higher pressures. The slope of the predicted phase boundary remains slightly different from the experimentally determined slope but similar to the slope predicted by the pretrained model. This similarity indicates that the predicted volumes for the phases are approximately preserved as intended. Thus, correcting the predicted volume can be necessary to further improve the agreement with experimental data. However, given accurate experimental references, such agreement can be ensured prior to the DiffTTC refinement using, e.g., the DiffTRe method [26]. Thus, incorporating the DiffTTC method into top-down training can tune the phase stability predicted for MLPs to align with experimental targets.
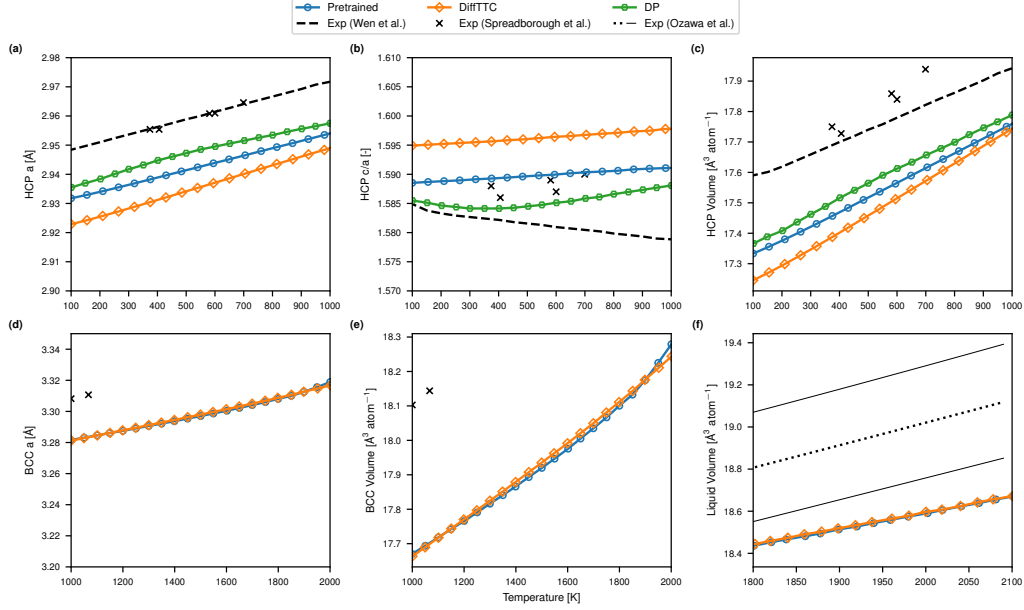
Figure 4: **Lattice Parameters and Volumes:** Predictions of the pretrained and refined MACE model are shown in comparison to the DP model [7] and experimental measurements. The values for the DP model and the experimental data corresponding to the black dashed lines in figures **(a-b)** are extracted from Wen et al. [7]. The black crosses are taken from J Spreadborough and J W Christian [53]. The regression line (dotted black) and uncertainty estimates (solid black) in plot (f) are converted from density measurements from Ozawa et al. [54].

3.3. Predicted Lattice Constants and Volumes

The molar volumes affect the slope and thus the alignment between the predicted and experimental reference phase boundaries. Moreover, we optimized the Helmholtz Free Energy in equation (6) instead of the Gibbs Free Energy based on the assumption that the pretrained and DiffTTC-refined MLPs predict similar volumes. Therefore, we predict the volumes and lattice constants of the HCP, BCC, and liquid phases at multiple temperatures and zero pressure to assess whether our pressure penalty is effective. Figure 4 displays the predictions of the pretrained and DiffTTC-refined MLP in comparison to experimental measurements and values for the DP model reported in Wen et al. [7].

The volumes predicted by the pretrained and DiffTTC-refined models closely agree over a wide temperature range for both the BCC and liquid phases, as well as for temperatures near the coexistence temperature for the HCP phase. Thus, the pressure penalty in the loss effectively preserves the predicted volumes at the coexistence temperature. However, the predicted volumes for the HCP phase increasingly differ with lower tempera-

15

tures. Moreover, the refined model predicts different HCP lattice constants than the pretrained model. These issues can arise from using the isotropic pressure in the pressure penalty. While the refined model predicts a similar average, resulting in a preserved volume, anisotropic stress leads to deformation of the box. Thus, while the current pressure penalty is sufficiently effective to ensure an approximately equal change in Gibbs and Helmholtz free energy, an anisotropic pressure penalty could better preserve lattice constants.

Comparing the predicted volumes to experimental data, both the pretrained and refined models underestimate the volumes for all phases. These deviations are specifically prominent at low temperatures, where quantum effects neglected by classical MD simulations become prominent [55]. These effects can be modeled via Path-Integral MD simulations, but become insignificant at higher temperatures above $400 - 700$ K [56]. For all temperatures, the HCP volumes predicted by the pretrained and DiffTTC-refined model are closer to the DP prediction than the DP prediction is to the experimental reference. These deviations between the MLPs and experimental reference can be due to the accuracy of DFT calculations, which typically deviate from experimental lattice constants in a magnitude of tenths up to a few % [55]. Thus, algorithms such as DiffTRe [26] could improve the volumes predicted by the MLPs based on experimental data, thereby potentially aligning the slopes of the predicted phase boundaries.

3.4. Out-of-Target Properties

We evaluate structural and dynamic properties for the liquid state of titanium to assess how the DiffTTC method affects out-of-target properties. Therefore, we compute the radial distribution function (RDF), angular distribution function (ADF), and diffusion constants displayed in Figure 5. Details on the computation are given in Supplementary Note 6.

The RDF and ADF predicted by the pretrained and DiffTTC-refined MLP are equal to each other up to line thickness. This result is consistent with previous studies, that many off-target properties are not affected when top-down training highly descriptive MLPs [26, 27]. Moreover, the predicted RDFs and ADFs closely agree with experimental references. Although predictions do not match the experimental reference up to line thickness, the predicted peaks are closely aligned. Only the absolute values for the reference data are slightly lower than predicted by the MLPs. The MLP-predicted diffusion constants differ more pronouncedly. The pretrained MLP slightly overstimates the diffusion compared to the experimental reference. On the other hand, the DiffTTC-refined model predicts a lower diffusion constant in good agreement with the reference In the given example of self-diffusion,
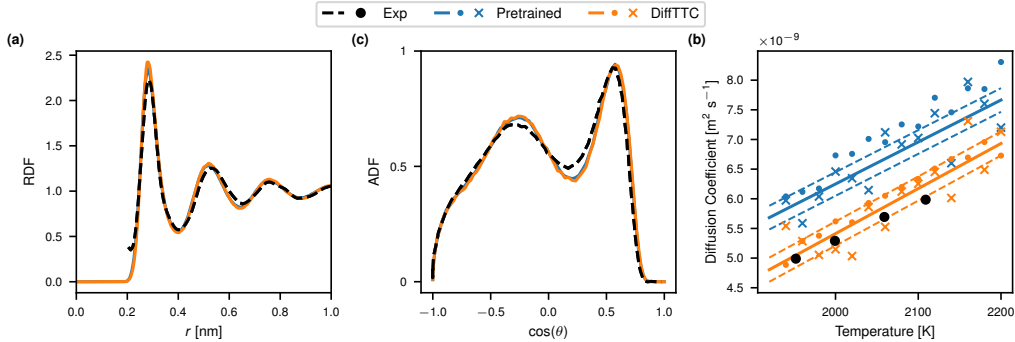
16

Figure 5: **Out-of-Target Properties for Liquid Titanium. a** Radial Distribution Function (RDF) and Angular Distribution Function (ADF) predicted for the pretrained and DiffTTC potential at 0 GPa and 1960 K in comparison to experimental measurements for RDF [57] and ADF [58]. **b** Diffusion constant at 0 GPa estimated for the pretrained and DiffTTC potential through velocity autocorrelation function (VACF, crosses) and temporal evolution of mean-squared displacement (points) in comparison to the experimental reference data [59] (black points). The solid lines are a linear regression fit to the VACF measurements. The dashed lines denote two times the standard error of the regression line offset.

we can observe that refining the MLP through DiffTTC can have a positive impact on out-of-target dynamical properties.

4. Discussion

In this paper, we presented a method to correct an MLP to accurately reproduce experimentally determined phase stabilities. Our method, DiffTTC, utilizes the DiffTRe algorithm to correct the free energy difference between two phases at the target pressure and temperature, ensuring that the thermodynamic criterion for the phases is fulfilled. We tested our method on the example of pure Titanium, correcting the phase boundary of the HCP, BCC, and liquid phases in a pressure range from 0 to 5 GPa.

We demonstrated that our method can align the MLP-predicted phase diagram with an experimental reference. Our presented DiffTTC-refined model significantly outperformed multiple reference models, including the pretrained baseline, the DP model from Wen et al. [7], and the foundational MACE-MP-0b3 [15] model. The remaining minor deviations in the slope with respect to the experimentally determined phase boundary could potentially be resolved by correcting the model prior to the DiffTTC method to match experimentally determined lattice constants and molar volumes. The DiffTTC method did not degrade the quality of the tested out-of-target properties. The RDF and ADF in the liquid phase predicted by the DiffTTC-refined model remained close to those predicted by the pretrained baseline

17

model and in good agreement with experimental data. Moreover, in the example of the diffusion constant, we could even observe a better agreement with experiments after correcting the phase boundaries.

Our method is independent of the procedure to compute the free energy difference between two phases for the initial MLP. As long as the isolated phases remain stable at constant temperature and volume on the timescale of practical MD simulation, the DiffTTC method can refine the phases' free energy. Thus, our method is directly applicable to more complex systems, such as binary or ternary phase transitions or phases with constant defect concentration. Based on DiffTRe, our method is highly flexible in regard to computational efficiency and compatibility with other training approaches. For example, simultaneously refining the MLP on mechanical properties [27] or structural properties [26] is straightforward. Moreover, enhanced sampling strategies such as population-based MD simulations [60] could be used instead of largely sequential MD simulations for trajectory recomputations.

Our results strengthen the opinion that top-down training is a highly valuable addition to the common Force Matching training of MLPs [18, 27, 28]. Problem-specific and foundational MLPs face multiple challenges in the dataset generation that often lead to a significant mismatch between predicted and experimentally determined material properties. Our DiffTTC method is a promising approach to overcoming these issues through top-down learning due to its high flexibility. In combination with a broad and accurate experimental dataset of molar volumes, as well as unary, binary, and potentially ternary phase diagrams, e.g., reliably collected in robotic laboratories, the DiffTTC method could highly improve the accuracy of foundational MLPs. These models might then reliably predict phase diagrams that are difficult to access experimentally.

In future work, we therefore aim to test the DiffTTC method for multi-component systems and train an accurate and transferable MLP. Therefore, we plan to test whether pretraining the MLP on volume data or matching the Gibbs Free Energy in the isobaric-isothermal ensemble might correct the slopes of the phase boundaries. Moreover, we plan to test whether data from the same phase across different temperatures and pressures can be shared or reused to reduce the computational cost associated with running molecular dynamics simulations independently for each temperature and pressure.

CRediT

Paul Fuchs: Conceptualization, Methodology, Software, Formal analysis, Investigation, Visualization, Writing - Original Draft. **Julija Zavadlav:**

Conceptualization, Validation, Writing - Review & Editing, Resources, Funding acquisition, Supervision, Project Administration.

Acknowledgements

Data and Code Availability

The DFT Ti-dataset [7] in curated form is publicly available at `https://github.com/tummfm/Fused-EXP-DFT-MLP`. The experimental phase transition data were extracted from Wen et al. [7]. The MD software LAMMPS and the training software `chemtrain` are publicly available at `https://github.com/lammps/lammps` and `https://github.com/tummfm/chemtrain`. The training and evaluation scripts will be made publicly available at `https://github.com/tummfm/DiffTTC` upon acceptance of the manuscript.

References

[1] S. Krouna, A. Acheche, G. Wang, N. O. Pena, R. Gatti, C. Ricolleau, H. Amara, J. Nelayah, D. Alloyeau, Atomic-Scale Insights Into the Thermal Stability of High-Entropy Nanoalloys, Advanced Materials 37 (2025) 2414510. doi:`10.1002/adma.202414510`.

[2] Q. Bizot, O. Politano, V. Turlo, F. Baras, Molecular dynamics simulations of nanoscale solidification in the context of Ni additive manufacturing, Materialia 27 (2023) 101639. doi:`10.1016/j.mtla.2022.101639`.

[3] A. Mahata, M. Asle Zaeem, Effects of solidification defects on nanoscale mechanical properties of rapid directionally solidified Al-Cu Alloy: A large scale molecular dynamics study, Journal of Crystal Growth 527 (2019) 125255. doi:`10.1016/j.jcrysgro.2019.125255`.

[4] D. E. Farache, J. C. Verduzco, Z. D. McClure, S. Desai, A. Strachan, Active learning and molecular dynamics simulations to find high melting temperature alloys, Computational Materials Science 209 (2022) 111386. doi:`10.1016/j.commatsci.2022.111386`.

[5] A. Del Masto, J. Baccou, G. Tréglia, F. Ribeiro, C. Varvenne, Insights on the capabilities and improvement ability of classical many-body potentials: Application to α-zirconium, Computational Materials Science 231 (2024) 112544. doi:10.1016/j.commatsci.2023.112544.

[6] J.-R. Castillo-Sánchez, A. Rincent, A. E. Gheribi, J.-P. Harvey, On the transferability of classical pairwise additive atomistic force field to the description of unary and multi-component systems: Applications to the solidification of Al-based alloys, Physical Chemistry Chemical Physics 24 (2022) 22605–22623. doi:10.1039/D2CP02746A.

[7] T. Wen, R. Wang, L. Zhu, L. Zhang, H. Wang, D. J. Srolovitz, Z. Wu, Specialising neural network potentials for accurate properties and application to the mechanical response of titanium, npj Computational Materials 7 (2021) 1–11. doi:10.1038/s41524-021-00661-y.

[8] C. Sun, D. Xue, Crystallization: A phase transition process driving by chemical potential decrease, Journal of Crystal Growth 470 (2017) 27–32. doi:10.1016/j.jcrysgro.2017.04.009.

[9] L. Zhang, J. Han, H. Wang, R. Car, W. E, Deep Potential Molecular Dynamics: A Scalable Model with the Accuracy of Quantum Mechanics, Physical Review Letters 120 (2018) 143001. doi:10.1103/PhysRevLett.120.143001.

[10] A. Musaelian, S. Batzner, A. Johansson, L. Sun, C. J. Owen, M. Kornbluth, B. Kozinsky, Learning local equivariant representations for large-scale atomistic dynamics, Nature Communications 14 (2023) 579. doi:10.1038/s41467-023-36329-y.

[11] I. Batatia, D. P. Kovács, G. N. C. Simm, C. Ortner, G. Csányi, MACE: Higher order equivariant message passing neural networks for fast and accurate force fields, 2022. arXiv:2206.07697.

[12] P. Fuchs, W. Chen, S. Thaler, J. Zavadlav, chemtrain-deploy: A Parallel and Scalable Framework for Machine Learning Potentials in Million-Atom MD Simulations, Journal of Chemical Theory and Computation (2025). doi:10.1021/acs.jctc.5c00996.

[13] Z. Zhao, M. Yi, W. Guo, Z. Zhang, General-purpose neural network potential for Ti-Al-Nb alloys towards large-scale molecular dynamics with ab initio accuracy, Physical Review B 110 (2024) 184115. doi:10.1103/PhysRevB.110.184115.

[14] S. Menon, Y. Lysogorskiy, A. L. M. Knoll, N. Leimeroth, M. Poul, M. Qamar, J. Janssen, M. Mrovec, J. Rohrer, K. Albe, J. Behler, R. Drautz, J. Neugebauer, From electrons to phase diagrams with machine learning potentials using pyiron based automated workflows, npj Computational Materials 10 (2024) 261. doi:`10.1038/s41524-024-01441-0`.

[15] I. Batatia, P. Benner, Y. Chiang, A. M. Elena, D. P. Kovács, J. Riebesell, X. R. Advincula, M. Asta, M. Avaylon, W. J. Baldwin, F. Berger, N. Bernstein, A. Bhowmik, F. Bigi, S. M. Blau, V. Cărare, M. Ceriotti, S. Chong, J. P. Darby, S. De, F. D. Pia, V. L. Deringer, R. Elijošius, Z. El-Machachi, F. Falcioni, E. Fako, A. C. Ferrari, J. L. A. Gardner, M. J. Gawkowski, A. Genreith-Schriever, J. George, R. E. A. Goodall, J. Grandel, C. P. Grey, P. Grigorev, S. Han, W. Handley, H. H. Heenen, K. Hermansson, C. Holm, C. H. Ho, S. Hofmann, J. Jaafar, K. S. Jakob, H. Jung, V. Kapil, A. D. Kaplan, N. Karimitari, J. R. Kermode, P. Kourtis, N. Kroupa, J. Kullgren, M. C. Kuner, D. Kuryla, G. Liepuoniute, C. Lin, J. T. Margraf, I.-B. Magdău, A. Michaelides, J. H. Moore, A. A. Naik, S. P. Niblett, S. W. Norwood, N. O'Neill, C. Ortner, K. A. Persson, K. Reuter, A. S. Rosen, L. A. M. Rosset, L. L. Schaaf, C. Schran, B. X. Shi, E. Sivonxay, T. K. Stenczel, V. Svahn, C. Sutton, T. D. Swinburne, J. Tilly, C. van der Oord, S. Vargas, E. Varga-Umbrich, T. Vegge, M. Vondrák, Y. Wang, W. C. Witt, T. Wolf, F. Zills, G. Csányi, A foundation model for atomistic materials chemistry, 2025. `arXiv:2401.00096`.

[16] B. M. Wood, M. Dzamba, X. Fu, M. Gao, M. Shuaibi, L. Barroso-Luque, K. Abdelmaqsoud, V. Gharakhanyan, J. R. Kitchin, D. S. Levine, K. Michel, A. Sriram, T. Cohen, A. Das, A. Rizvi, S. J. Sahoo, Z. W. Ulissi, C. L. Zitnick, UMA: A family of universal models for atoms, 2025. `arXiv:2506.23971`.

[17] A. Mazitov, F. Bigi, M. Kellner, P. Pegolo, D. Tisi, G. Fraux, S. Pozdnyakov, P. Loche, M. Ceriotti, PET-MAD as a lightweight universal interatomic potential for advanced materials modeling, Nature Communications 16 (2025) 10653. doi:`10.1038/s41467-025-65662-7`.

[18] S. Mannan, V. Bihani, C. Gonzales, K. L. K. Lee, N. N. Gosvami, S. Ranu, S. Miret, N. M. A. Krishnan, Evaluating universal machine learning force fields against experimental measurements, 2025. `arXiv:2508.05762`.

[19] Y. Liu, X. He, Y. Mo, Discrepancies and error evaluation metrics for machine learning interatomic potentials, npj Computational Materials 9 (2023) 174. doi:10.1038/s41524-023-01123-3.

[20] D. Kuryla, F. Berger, G. Csányi, A. Michaelides, How accurate are DFT forces? Unexpectedly large uncertainties in molecular datasets, 2025. arXiv:2510.19774.

[21] G. Imbalzano, M. Ceriotti, Modeling the Ga/As binary system across temperatures and compositions from first principles, Physical Review Materials 5 (2021) 063804. doi:10.1103/PhysRevMaterials.5.063804.

[22] F. Dorner, Z. Sukurma, C. Dellago, G. Kresse, Melting Si: Beyond Density Functional Theory, Physical Review Letters 121 (2018) 195701. doi:10.1103/PhysRevLett.121.195701.

[23] L.-F. Zhu, B. Grabowski, J. Neugebauer, Efficient approach to compute melting properties fully from ab initio with application to Cu, Physical Review B 96 (2017) 224202. doi:10.1103/PhysRevB.96.224202.

[24] L.-F. Zhu, F. Körmann, A. V. Ruban, J. Neugebauer, B. Grabowski, Performance of the standard exchange-correlation functionals in predicting melting properties fully from first principles: Application to Al and magnetic Ni, Physical Review B 101 (2020) 144108. doi:10.1103/PhysRevB.101.144108.

[25] J. S. Smith, B. T. Nebgen, R. Zubatyuk, N. Lubbers, C. Devereux, K. Barros, S. Tretiak, O. Isayev, A. E. Roitberg, Approaching coupled cluster accuracy with a general-purpose neural network potential through transfer learning, Nature Communications 10 (2019) 2903. doi:10.1038/s41467-019-10827-4.

[26] S. Thaler, J. Zavadlav, Learning neural network potentials from experimental data via Differentiable Trajectory Reweighting, Nature Communications 12 (2021) 6884. doi:10.1038/s41467-021-27241-4.

[27] S. Röcken, J. Zavadlav, Accurate machine learning force fields via experimental and simulation data fusion, npj Computational Materials 10 (2024) 1–10. doi:10.1038/s41524-024-01251-4.

[28] S. Röcken, A. F. Burnet, J. Zavadlav, Predicting solvation free energies with an implicit solvent machine learning potential, The Journal of Chemical Physics 161 (2024) 234101. doi:10.1063/5.0235189.

[29] R. W. Zwanzig, High-Temperature Equation of State by a Perturbation Method. I. Nonpolar Gases, The Journal of Chemical Physics 22 (1954) 1420–1426. doi:10.1063/1.1740409.

[30] G. M. Torrie, J. P. Valleau, Nonphysical sampling distributions in Monte Carlo free-energy estimation: Umbrella sampling, Journal of Computational Physics 23 (1977) 187–199. doi:10.1016/0021-9991(77)90121-8.

[31] T. D. Swinburne, C. Lapointe, M.-C. Marinica, Agnostic calculation of atomic free energies with the descriptor density of states, 2025. arXiv:2502.18191.

[32] C. Vega, E. Sanz, J. L. F. Abascal, E. G. Noya, Determination of phase diagrams via computer simulation: Methodology and applications to water, electrolytes and proteins, Journal of Physics: Condensed Matter 20 (2008) 153101. doi:10.1088/0953-8984/20/15/153101.

[33] M. E. Tuckerman, Statistical Mechanics: Theory and Molecular Simulation, Oxford Graduate Texts, reprinted (with corr.) ed., Oxford Univ. Press, Oxford, 2015.

[34] G. B. Correa, Y. Zhang, C. R. A. Abreu, F. W. Tavares, E. J. Maginn, Revisiting the pseudo-supercritical path method: An improved formulation for the alchemical calculation of solid–liquid coexistence, The Journal of Chemical Physics 159 (2023) 104105. doi:10.1063/5.0163564.

[35] D. Frenkel, A. J. C. Ladd, New Monte Carlo method to compute the free energy of arbitrary solids. Application to the fcc and hcp phases of hard spheres, The Journal of Chemical Physics 81 (1984) 3188–3193. doi:10.1063/1.448024.

[36] N. P. Schieber, E. C. Dybeck, M. R. Shirts, Using reweighting and free energy surface interpolation to predict solid-solid phase diagrams, The Journal of Chemical Physics 148 (2018) 144104. doi:10.1063/1.5013273.

[37] M. de Koning, A. Antonelli, S. Yip, Optimized Free-Energy Evaluation Using a Single Reversible-Scaling Simulation, Physical Review Letters 83 (1999) 3973–3977. doi:10.1103/PhysRevLett.83.3973.

[38] Y. Zhang, E. J. Maginn, A comparison of methods for melting point calculation using molecular dynamics simulations, The Journal of Chemical Physics 136 (2012) 144116. doi:10.1063/1.3702587.

[39] A. P. Thompson, H. M. Aktulga, R. Berger, D. S. Bolintineanu, W. M. Brown, P. S. Crozier, P. J. in 't Veld, A. Kohlmeyer, S. G. Moore, T. D. Nguyen, R. Shan, M. J. Stevens, J. Tranchida, C. Trott, S. J. Plimpton, LAMMPS - a flexible simulation tool for particle-based materials modeling at the atomic, meso, and continuum scales, Computer Physics Communications 271 (2022) 108171. doi:10.1016/j.cpc.2021.108171.

[40] M. de Koning, Optimizing the driving function for nonequilibrium free-energy calculations in the linear regime: A variational approach, The Journal of Chemical Physics 122 (2005) 104106. doi:10.1063/1.1860556.

[41] R. Freitas, M. Asta, M. de Koning, Nonequilibrium free-energy calculation of solids using LAMMPS, Computational Materials Science 112 (2016) 333–341.

[42] O. T. Unke, S. Chmiela, H. E. Sauceda, M. Gastegger, I. Poltavsky, K. T. Schütt, A. Tkatchenko, K.-R. Müller, Machine Learning Force Fields, Chemical Reviews 121 (2021) 10142–10186. doi:10.1021/acs.chemrev.0c01111.

[43] I. Batatia, S. Batzner, D. P. Kovács, A. Musaelian, G. N. C. Simm, R. Drautz, C. Ortner, B. Kozinsky, G. Csányi, The design space of E(3)-equivariant atom-centred interatomic potentials, Nature Machine Intelligence 7 (2025) 56–67. doi:10.1038/s42256-024-00956-x.

[44] F. Ercolessi, J. B. Adams, Interatomic Potentials from First-Principles Calculations: The Force-Matching Method, Europhysics Letters (EPL) 26 (1994) 583–588. doi:10.1209/0295-5075/26/8/005.

[45] S. P. Carmichael, M. S. Shell, A New Multiscale Algorithm and Its Application to Coarse-Grained Peptide Models for Self-Assembly, The Journal of Physical Chemistry B 116 (2012) 8383–8393. doi:10.1021/jp2114994.

[46] C. H. Bennett, Efficient estimation of free energy differences from Monte Carlo data, Journal of Computational Physics 22 (1976) 245–268. doi:10.1016/0021-9991(76)90078-4.

[47] D. P. Kingma, J. Ba, Adam: A Method for Stochastic Optimization, 2017. arXiv:1412.6980.

[48] S. Thaler, M. Stupp, J. Zavadlav, Deep coarse-grained potentials via relative entropy minimization, The Journal of Chemical Physics 157 (2022) 244103. doi:10.1063/5.0124538.

[49] P. M. Larsen, S. Schmidt, J. Schiøtz, Robust structural identification via polyhedral template matching, Modelling and Simulation in Materials Science and Engineering 24 (2016) 055007. doi:10.1088/0965-0393/24/5/055007.

[50] S. Goswami, S. Jensen, Y. Yang, M. Holzmann, C. Pierleoni, D. M. Ceperley, High temperature melting of dense molecular hydrogen from machine-learning interatomic potentials trained on quantum Monte Carlo, The Journal of Chemical Physics 162 (2025) 054118. doi:10.1063/5.0250686.

[51] D. Errandonea, B. Schwager, R. Ditz, C. Gessmann, R. Boehler, M. Ross, Systematics of transition-metal melting, Physical Review B 63 (2001) 132104. doi:10.1103/PhysRevB.63.132104.

[52] V. Stutzmann, A. Dewaele, J. Bouchet, F. Bottin, M. Mezouar, High-pressure melting curve of titanium, Physical Review B 92 (2015) 224110. doi:10.1103/PhysRevB.92.224110.

[53] J Spreadborough, J W Christian, The Measurement of the Lattice Expansions and Debye Temperatures of Titanium and Silver by X-ray Methods, Proceedings of the Physical Society 74 (1959) 609. doi:10.1088/0370-1328/74/5/314.

[54] S. Ozawa, Y. Kudo, K. Kuribayashi, Y. Watanabe, T. Ishikawa, Precise Density Measurement of Liquid Titanium by Electrostatic Levitator, MATERIALS TRANSACTIONS 58 (2017) 1664–1669. doi:10.2320/matertrans.L-M2017835.

[55] P. Hao, Y. Fang, J. Sun, G. I. Csonka, P. H. T. Philipsen, J. P. Perdew, Lattice constants from semilocal density functionals with zero-point phonon correction, Physical Review B 85 (2012) 014111. doi:10.1103/PhysRevB.85.014111.

[56] Z. Yan, C. Zhang, X. Liu, Q. Miao, M. Fang, W. Kang, Accurate path-integral molecular dynamics calculation of aluminum with improved empirical ionic potentials, Physical Review B 106 (2022) 174107. doi:10.1103/PhysRevB.106.174107.

[57] D. Holland-Moritz, O. Heinen, R. Bellissent, T. Schenk, Short-range order of stable and undercooled liquid titanium, Materials Science and Engineering: A 449–451 (2007) 42–45. doi:`10.1016/j.msea.2005.12.093`.

[58] T. H. Kim, K. F. Kelton, Structural study of supercooled liquid transition metals, The Journal of Chemical Physics 126 (2007) 054513. doi:`10.1063/1.2431173`.

[59] J. Horbach, R. E. Rozas, T. Unruh, A. Meyer, Improvement of computer simulation models for metallic melts via quasielastic neutron scattering: A case study of liquid titanium, Physical Review B 80 (2009) 212203. doi:`10.1103/PhysRevB.80.212203`.

[60] H. Christiansen, M. Weigel, W. Janke, Accelerating Molecular Dynamics Simulations with Population Annealing, Physical Review Letters 122 (2019) 060602. doi:`10.1103/PhysRevLett.122.060602`.

[61] Jülich Supercomputing Centre, JUWELS Cluster and Booster: Exascale Pathfinder with Modular Supercomputing Architecture at Juelich Supercomputing Centre, Journal of large-scale research facilities 7 (2021). URL: `http://dx.doi.org/10.17815/jlsrf-7-183`. doi:`10.17815/jlsrf-7-183`.